Annu. Rev. Mater. Sci. 1996. 26:551–79

RAMAN SPECTROSCOPY FOR CHARACTERIZATION OF HARD, WIDE-BANDGAP SEMICONDUCTORS: Diamond, GaN, GaAlN, AlN, BN

Leah Bergman and Robert J. Nemanich

Department of Physics and Department of Materials Science and Engineering, North Carolina State University, Raleigh, North Carolina 27695-8202

KEY WORDS: Raman lineshape, diamond films, stress, temperature

ABSTRACT

This paper reviews the Raman spectroscopy of diamond films, GaN, $Al_xGa_{1-x}N$ alloys, AlN, and BN. The review focuses on the use of Raman spectroscopy to characterize various physical aspects such as stress, temperature, and microstructure, as determined by their influence on the Raman active modes manifested by the Raman lineshape. The phonon-plasmon interaction in GaN due to the characteristic unintentional *n*-type doping of this material is also discussed. Furthermore, a short summary of the behavior of the optical modes of mixed alloys is presented, followed by a discussion of the Raman characteristics of $Al_xGa_{1-x}N$ alloy.

INTRODUCTION

Diamond, gallium nitride, aluminum nitride, and cubic boron nitride are of great potential in the development of novel optoelectronic devices owing to their wide-bandgap and superior mechanical and thermal prop-

0084-6600/96/0801-0551$08.00

erties (1–6). Recent advances in the crystal growth techniques of diamond films (7–12) and the group III nitride materials (1, 3, 6, 13, 14) have enabled numerous studies via Raman spectroscopy.

The Raman effect in solids is due to inelastic scattering of light by the crystal vibrations (the latter are referred to as phonons or optical modes). The incident light exchanges a quantum of energy with the crystal via the creation or annihilation of phonons. As a result, the scattered light loses or gains an energy quantum depending on whether a phonon was created or annihilated. In Raman spectroscopy, the shift of the energy of the scattered light is measured: Thus a characteristic value of the vibrational energy of a given solid may be obtained. The characteristic Raman energy, known as the Raman frequency, may be modified from its ideal value (corresponding to high quality material) by, among other factors, stress, temperature, structural defects, and impurities. Thus Raman spectroscopy may yield valuable information on the material characteristics and quality.

This paper reviews the use of Raman spectroscopy to characterize a family of wide-bandgap materials that includes diamond and members from the group III nitrides. We focus on issues of stress (15), temperature (16), microstructure (17), and free carriers (18–21).

First we review the applications of Raman spectroscopy to diamond films. The issue of the identification of the coexisting diamond and graphitic phases in diamond films is discussed, as well as that of the Raman lineshape of the diamond and the physical mechanisms affecting it. Next we summarize the Raman modes of the hexagonal wurtzite (WZ) and the cubic zinc-blend polytype structures of GaN. The effect of pressure and free carriers on Raman frequency of the WZ structure is examined. A review of the Raman characteristics of $Al_xGa_{1-x}N$ alloy is presented. Raman-active modes of the wurtzite AlN and the effect of applied pressure on the Raman frequencies are reviewed. The effect of oxygen impurity on the Raman characteristics is also considered. Finally the bonding-anisotropy of the h-BN and the effect of the crystallite size on the Raman modes is discussed along with the effect of high pressure and temperature on the Raman frequencies of h-BN and c-BN.

RAMAN SPECTROSCOPY OF DIAMOND FILMS

The issues considered are the identification of the coexisting diamond and graphitic phases in diamond films and the effect of the graphitic phase on the film quality. Also addressed is the issue of the Raman lineshape of the diamond and the physical mechanisms affecting it.

Identification of Bonding Configurations

Important applications of Raman spectroscopy to diamond films are the identification of the diamond structure and the amorphous structure of the sp^2 carbon (graphitic phase) that coexist in many of the diamond films (22–24). Shroder et al (23) have developed a model in which the concentrations of diamond and graphitic components in diamond films may be obtained from the Raman intensities. The following section outlines the principal results.

The Raman intensity from a material I (in a backscattering geometry) has been shown by Loudon (25) to follow the relation:

$$I = \frac{I_0 S}{S + \alpha_1 + \alpha_2}\{1 - \exp[-(S + \alpha_1 + \alpha_2)L]\},$$

where S is the scattering efficiency, I_0 is the incident intensity, L is the sample thickness in the direction of the incident laser light, and α_1 and α_2 are the absorption coefficients at the frequencies of the incident and scattered light, respectively. Wada & Solin (26) showed that the equation could be modified to give the ratio of the Raman intensities of two different materials:

$$\frac{I_D}{I} = \frac{I_{0D}}{I_0}\left[\frac{A_D}{A}\right]\left[\frac{L_D(\alpha_1 + \alpha_2)}{1}\right]\left[\frac{\Delta\Omega_D}{\Delta\Omega}\right]\left[\frac{1 - R_D}{1 - R}\right]^2 \times \left[\frac{\{\sum_j (\hat{\mathbf{e}}_2 \cdot \mathbf{R}_j \cdot \hat{\mathbf{e}}_1)^2\}_D}{\{\sum_j (\hat{\mathbf{e}}_2 \cdot \mathbf{R}_j \cdot \hat{\mathbf{e}}_1)^2\}}\right], \quad 1.$$

where S has been redefined in terms of a scattering efficiency (A) and a summation over the inner produce of the Raman tensor ($\mathbf{R}_j$) and the polarization unit vectors of the incident and scattered light $\hat{\mathbf{e}}_1$ and $\hat{\mathbf{e}}_2$. I is the scattering intensity of the material being compared; I_D represents the scattered intensity from the diamond, and I_0 is the incident intensity. $\Delta\Omega$ is the solid angle into which light is scattered, and the term involving R is a correction term for reflection of the scattered light at the sample surface and multiple reflections within the sample. Here, α_1 and α_2 are the previously defined absorption coefficients of the material to be compared with diamond because diamond is assumed to be transparent to the visible laser radiation.

In order to investigate the Raman intensity from a composite, Shroder et al (23) prepared samples consisting of compressed powder of ~1 μm diamond and ~40 μm graphite particles for which the concentrations in each sample were known. In order to apply Equation 1 to the diamond-

graphite composite samples, several approximations relevant to the experimental conditions were made. The first approximation was that the values of L_D and $\Delta\Omega$ were the same for both materials because the Raman signal was being collected from a region of discrete particles. Moreover, the reflection losses due to light scattering between the graphite and diamond particles were assumed to be minimal and thus were disregarded. Finally, due to the random orientations of the particles, an angle-average value of the summation over all possible polarization directions was taken.

In light of these approximations, the ratio of the Raman scattering intensities of diamond to graphite may be given as

$$\frac{I_D}{I_G} = \frac{4A'_D N_D V_D}{3A'_G N_G V'_G} = \frac{4A'_D N_D V_D}{3A'_G N_G V_G}\left[\frac{V_G}{V'_G}\right], \qquad 2.$$

where A' is the angle- and polarization-averaged scattering efficiency per nearest-neighbor bond, N is the atomic density, and V_D is the volume of the diamond, which is sampled by the Raman scattering. The absorption factor of graphite is accounted for in the V'_G/V_G term, which represents the fraction of each graphite particle sampled in the Raman process. Apportioning the volume of diamond is not applicable because it is essentially transparent to the laser light, and thus the entire volume of diamond is sampled by the Raman scattering. The factor of 4/3 accounts for diamond having four nearest-neighbors and graphite having three nearest-neighbors at each site. Equation 2 can be written in terms of the percentage of diamond in the composites P_D as follows:

$$\frac{I_D}{I_G} \sim \frac{4A'_D}{3A'_G}\left[\frac{P_D}{1 - P_D}\right]\left[\frac{V_G}{V'_G}\right]. \qquad 3.$$

At 514.5-nm laser excitation, graphite has an absorption depth of ~30 nm (26). However, because the scattered light must also exit the absorption region, an absorption length of ~15 nm was considered instead (see Figure 1*a*). The ratio of the scattering efficiencies A'_D/A'_G was taken to be ~1/75 (26).

Equation 3 states that for a given composite the relative Raman intensities are modulated not only by the relative Raman scattering efficiency but also by the volume of the absorbing component, which is actually sampled by Raman scattering. The effect of the absorption on the Raman spectra can be seen qualitatively in the spectra presented in Figure 1*b*. The spectra of diamond-graphite composites (of ~1 μm diamond and ~40 μm graphite particles) is shown for which the relative concentration of diamond in the samples ranges from ~1 up to 60%. An

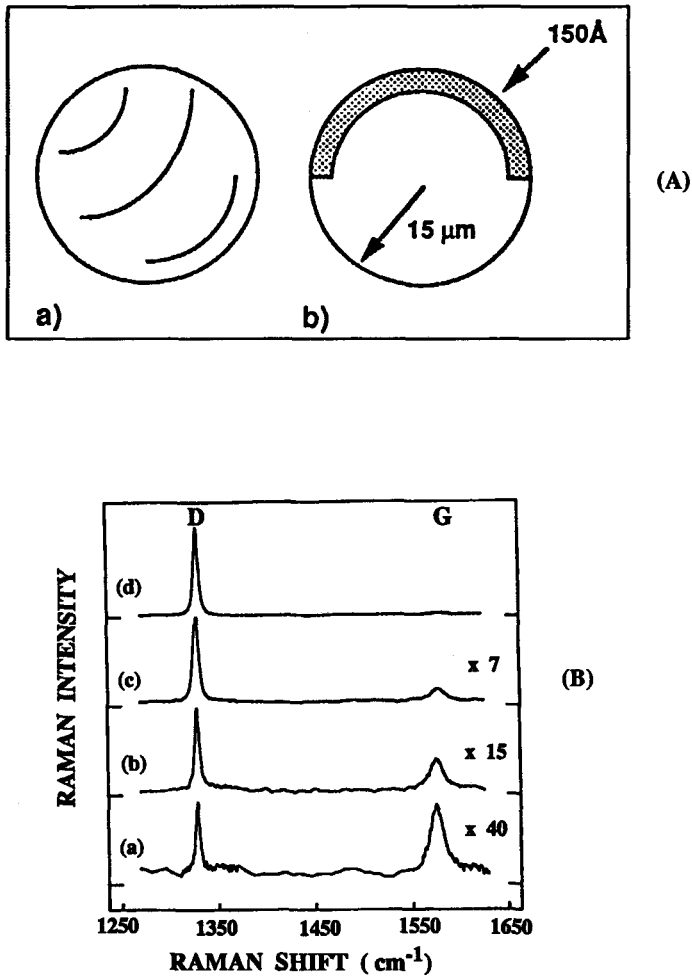

Figure 1 *(A)* Model of the unit volumes in the Raman scattering from composites: *(a)* fully illuminated diamond particle of ~30 μm size and *(b)* graphite particle ~30 μm size, partially illuminated in a 15 nm surface layer. *(B)* The Raman spectra of the composites of diamond and graphite powders. The relative concentrations of diamond in the samples are *(a)* 1.3%, *(b)* 6.6%, *(c)* 21.5%, and *(d)* 50%. The diamond band *(D)* is at 1332 cm^{-1} and the graphite band *(G)* is at 1580 cm^{-1}. (From 23.)

interesting aspect of these spectra is that the ~1% diamond composite displays a 1:1 ratio between the peak intensities of diamond and graphite. At 50% diamond concentration, the peak arising from graphite has practically disappeared even though the Raman cross section is 75 times

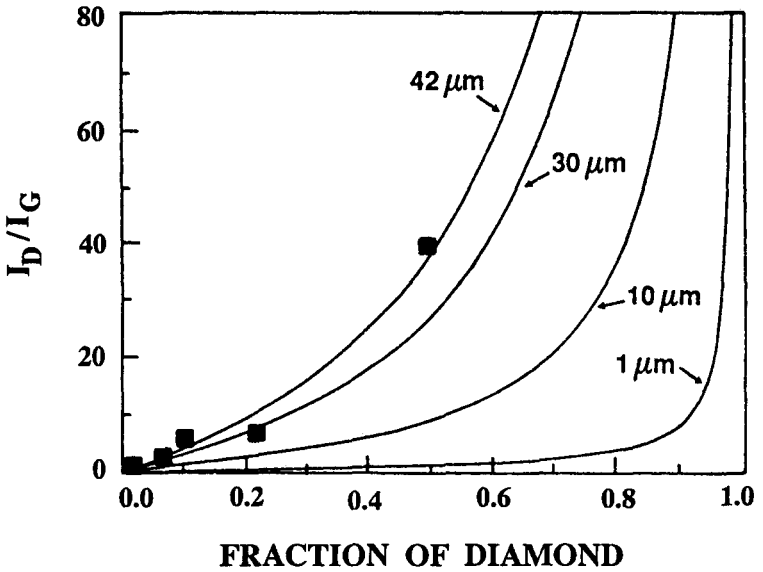

Figure 2 Ratio of peak intensities (I_D/I_G) vs relative concentration of diamond in the composite samples. The solid lines are derived from Equation 3, assuming an average graphite particle size of 42, 30, 10, and 1 μm, respectively. (From 23.)

larger in graphite than in diamond. Thus the absorption of graphite has a significant effect on the Raman spectra of the composites, as is shown in the large disparity of the measured intensities of the samples.

The quantitative predictions of the model, as given in Equation 3, are evidenced in Figure 2, where the ratio of the two peaks vs concentration of diamond is plotted for various particle sizes of graphite. It can be seen that when the particle size was taken to be 42 μm, the model and the experimental data are in agreement. Within the model, when the graphite domains are smaller than the absorption length, the value of V'_G/V_G becomes 1, and the effect of absorption can be ignored. The only intensity-modulation factor in that case is the relative Raman scattering efficiency. In high-quality diamond films, the graphitic domains are very small, so when applying the model, in most cases, the absorption effect may similarly be ignored.

Recent investigations of photoluminescence and Raman scattering in diamond thin films have shown that the graphitic phase affects the optical as well as the mechanical properties of the diamond (27–29). In many diamond films, a strong broadband luminescence extending from approximately 1.5 to 2.5 eV and centered at ~2 eV has been observed (30). The photoluminescence results from transitions of an

in-gap state-distribution, which has been attributed to the graphitic-disordered phase in the diamond films(28). Moreover, it has been determined that the internal compressive stress in diamond thin films is due to various impurities and defects present in the film, in particular due to the graphitic phase (29, 31).

The Diamond Raman Lineshape of Diamond Films

The Raman frequency of a high-quality material yields information about the vibrational energy of the phonons, whereas the Raman linewidth is a measure of the phonon lifetime. When the quality of a material is degraded by the presence of defects, the resulting Raman lineshape reflects the effect of the defects on the phonon characteristics. The focus of this section is recent investigations of Raman lineshape as it relates to the various defects present in diamond thin films.

The Raman linewidth in general can be broadened via several mechanisms: The main mechanisms applicable to the diamond line are homogeneous broadening (32) and broadening due to the size effect of the crystal, a theory that has been developed to explain the lineshape of boron-nitride material (17). Homogeneous broadening arises from a decrease of the lifetime of the crystal phonons. The theory of homogeneous spectral lineshape predicts that the linewidth is inversely proportional to the phonon lifetime and that the lineshape is expected to be a Lorentzian (33). The other mechanism that results in Raman line broadening is phonon confinement in a small domain size (17).

The well-established confinement model is based on the uncertainty principle $\Delta k \sim 2\pi/d$, which states that the smaller the domain size d, the larger the range of different phonons that are allowed to participate in the Raman process. Hence the broadening of the Raman line in this case is due to the spread in phonon energy, and the lineshape reflects the shape of the phonon-dispersion curve. The Raman lineshape in the phonon-confinement model is given by

$$I(w) \cong \int_0^1 \frac{dq \exp(-q^2L^2 / 4)4 \pi q^2}{[\omega - \omega(q)]^2 + (W_0 / 2)^2}, \qquad 4.$$

where L is the confinement size, W_0 is the diamond natural linewidth ($\sim 2\ cm^{-1}$), and $\omega(q)$ is the phonon-dispersion curve of the form A + B *cos($q\pi$), (17, 34–36). In general, the width, shape, and peak position are dependent on the specific character of phonon-dispersion curves. In particular for silicon, the above model predicts that as the crystalline domain size decreases, the peak of the Raman line shifts to a lower frequency and the lineshape becomes asymmetric (35).

Ager et al (34) have investigated the application of the confinement model to the Raman lineshape of diamond thin films. For each of the relevant phonon-dispersion relations, Ager et al modeled the expected lineshape using the confinement model (Equation 4) and compared the results with the Raman lineshape of diamond films. The study of the expected Raman line involved three sets of lineshape calculations in which different one-dimensional dispersion curves were used. First, in case (a), a dispersion relation was used for which the phonon frequency decreases away from the Γ point. The dispersion relation has the form $\omega(q) = A + B\cos(q\pi)$, where $A = 1241.24\ cm^{-1}$ and $B = 91.25\ cm^{-1}$; the shape of this curve is similar to that used in Si and GaAs phonon-confinement calculations. For case *(b)*, the Δ_2 (O) dispersion curve was used; this curve in diamond has a shallow maximum, which is farther from the Γ point. Figure 3 depicts the characteristics of the first two dispersion relations (37). Lastly, in case *(c)*, the weighted averaged three-dimensional dispersion curve was used in the calculations (see Reference 34 for a more detailed analysis).

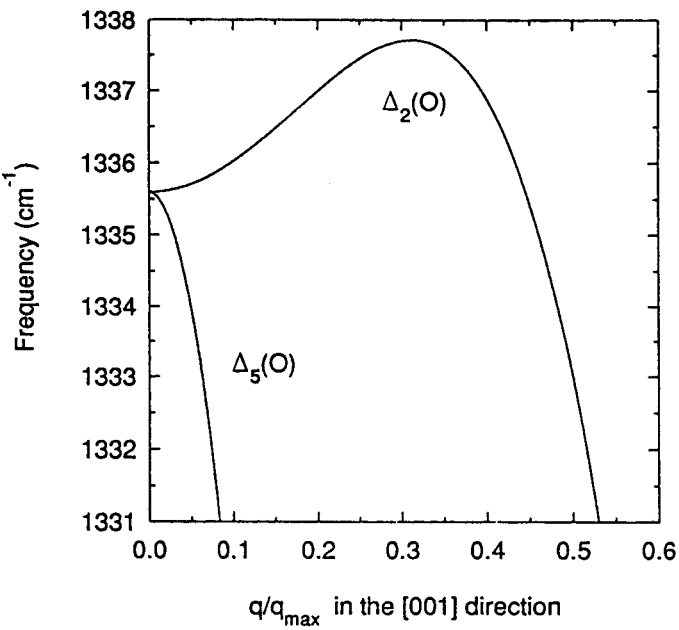

Figure 3 Detail of the (001) phonon-dispersion curves for diamond. The Δ_5(O) has a maximum at Γ point. The Δ_2(O) curve exhibits a shallow maximum away from the Γ point. (From 34, 37.)

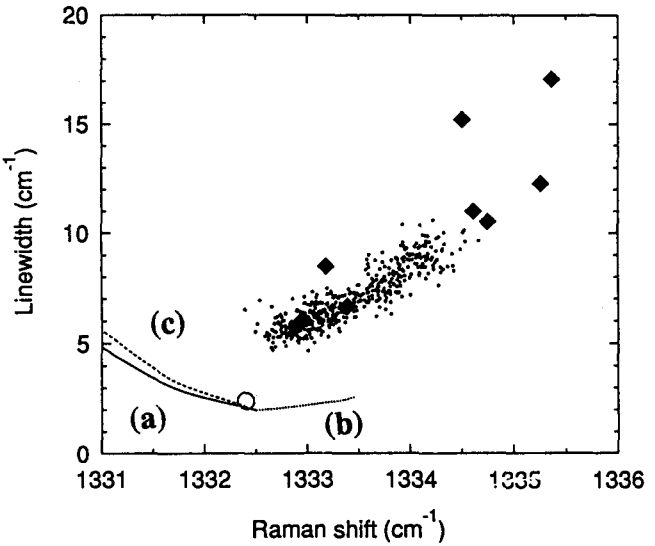

Figure 4 Raman linewidth vs Raman frequency for diamond: single-crystal *(circle)*; single-point measurements from ten diamond films *(diamonds)*; 500 spatially resolved measurements from one sample *(dots)*; phonon-confinement theory as predicted from case (*a*), the predicted model case (*b*), and of case (*c*). (From 34.)

Figure 4 presents the Raman linewidth vs the Raman frequency, as obtained from Equation 4, for the three cases of dispersion relations. Also presented in the figure is the correlation of the Raman linewidth vs frequency, which was obtained from diamond films. Figure 5 shows the predicted Raman lineshapes as calculated from the phonon-confinement theory for various values of domain size L for dispersion relations *(a)* and *(b)*. In Figure 6, the Raman spectra of diamond films and crystal are presented. As shown, there is significant disagreement between the Raman diamond lineshapes obtained from diamond films (which are symmetric) and those predicted from the confinement model (which are asymmetric). Moreover, the confinement model predicts a red shift of the Raman frequency as the line gets broader, which is opposite in behavior to the observed diamond peak frequencies.

From these results Ager et al have concluded that the size effect in diamond films is not a dominant factor in determining the lineshape characteristics of diamond films. They suggested that the internal compressive stress in diamond is a more likely mechanism in determining the Raman lineshape. Results similar to those obtained by Ager et al also have been reported by Bergman & Nemanich (29); moreover, in

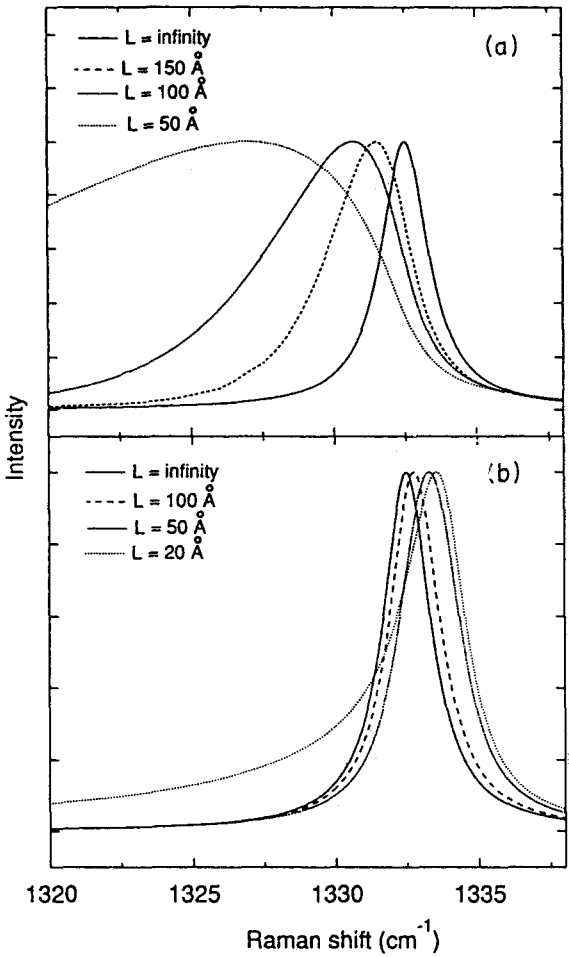

Figure 5 Calculated Raman lineshapes from the phonon-confinement theory for different values of domain size *L*. *(a)* Results when using dispersion relation described in case *(a)*, *(b)* the results of case *(b)*. (From 34.)

the latter study, the Raman lineshape was found to be correlated to the internal compressive stress imposed, for the most part, by the graphitic phase present in the diamond thin films.

Recently, a study of the Raman lineshape of nanometer-sized diamond particles was conducted by Yoshikawa et al (38). The diamond particles, referred to as cluster diamond, are produced via detonation of explosives and have promising potential in a variety of mechanical applications (38). The observed Raman spectrum of the cluster diamond

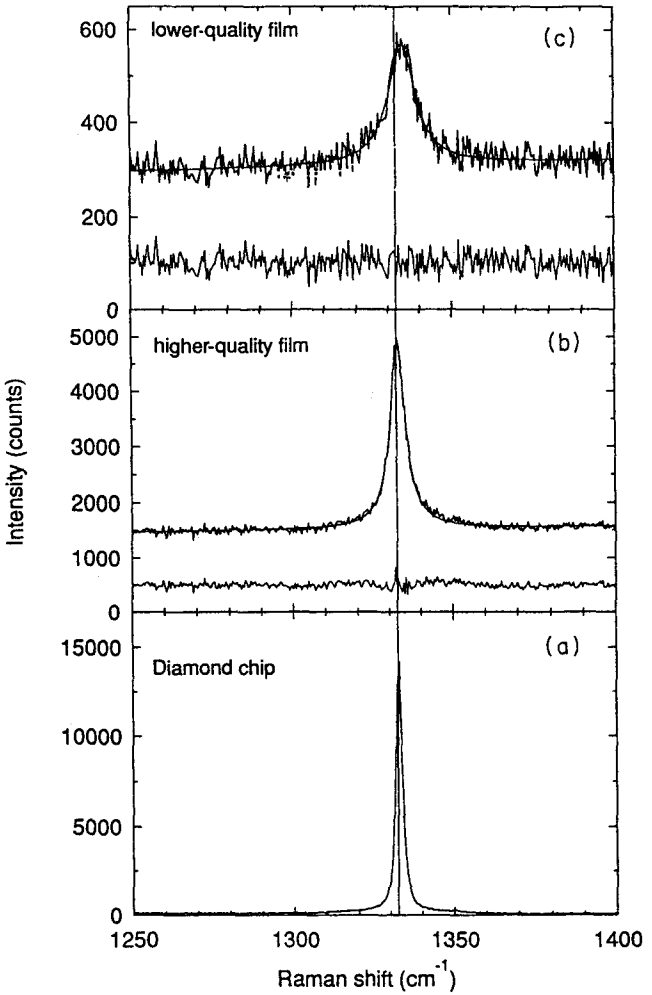

Figure 6 Raman spectra of diamonds. *(a)* Type IIa synthetic diamond. *(b)* High quality diamond film, and *(c)* lower-quality diamond film. The lines exhibit a Lorentzian lineshape. (From 34.)

has been found to agree with that calculated by the phonon-confinement model. A Raman spectrum and the calculated lineshape are presented in Figure 7, where the Raman frequency is 1320 cm^{-1} (which is a decrease from the 1332 cm^{-1} frequency of crystalline diamond or high-quality film); moreover, the lineshape of the cluster diamond is asymmetric. The particle size, which has been calculated via the confinement

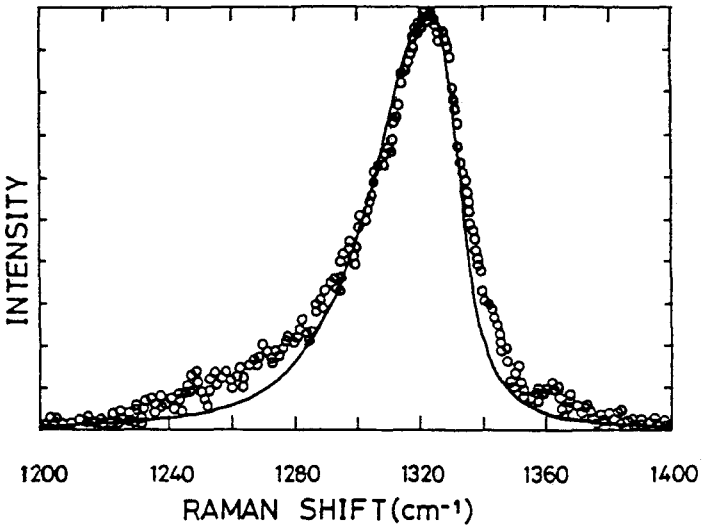

Figure 7 The Raman lineshape of cluster diamond; experimental data *(circles)* calculated line *(solid line)*. (From 38.)

model $L = 55$ Å, agrees with that estimated from X-ray measurements (38).

GALLIUM NITRIDE

In this section the Raman modes of the hexagonal wurtzite (WZ) and the cubic zinc-blend polytype structures of GaN are summarized. The effect of pressure and free carriers on Raman frequency and lineshape of the WZ structure is discussed. Lastly, a short summary of the behavior of the optical modes of mixed alloys is presented, followed by a discussion of the Raman characteristics of $Al_xGa_{1-x}N$ alloy.

GaN in the stable state has a wurtzite crystal structure and belongs to the space group C_{6v}^4. The group theory predicts that there are four Raman active modes represented by $A_1 + E_1 + 2E_2$ (39). The A_1 mode splits into longitudinal (LO) and transverse (TO) components, as does the E_1 mode; the two E_2 modes are nonpolar modes. Table 1 lists the observed Raman frequencies that have been reported (40–42).

The GaN samples investigated by Manchon et al (40) were in a crystalline form that was prepared by heating a pre-purified GaN powder at 1200°C. The A_1(LO) and the E_1(LO) modes investigated by Cingolani et al (41) were obtained from a crystalline sample and from an epitaxial GaN film grown on sapphire substrate, respectively. The

Table 1 The frequencies in units of cm^{-1} of the WZ gallium nitride Raman modes

$A_1(LO)$	$A_1(TO)$	$E_1(LO)$	$E_1(TO)$	$E_2^{(1)}$	$E_2^{(2)}$	Reference
—	533	—	559	145	568	40
710	—	741	—	—	—	41
738	—	—	—	—	570	42

samples investigated by Murugkar et al (42) were grown on c-plane (0001) sapphire substrates. The frequency of the A_1 (LO) mode reported by the latter group is blue shifted by 28 cm^{-1} from the A_1 (LO) at 710 cm^{-1} reported in Reference 41. The blue shift has been tentatively ascribed to effects due to stress in the film (42).

A detailed study of the effect of pressure on the crystalline GaN Raman lines has been reported (43). The applied pressure was hydrostatic in the range 0 to ~50 GPa. The pressure dependence of the Raman frequencies of the A_1 (TO), E_1 (TO), E_2^2, and E_2^1 modes has been shown to follow the quadratic relation:

$$\omega(cm^{-1}) = \omega_0 + \sigma_1 P + \sigma_2 P^2, \qquad 5.$$

where P is the applied pressure in units of GPa, ω_0 is the Raman frequency at zero applied pressure, and σ_1 and σ_2 are the first and second pressure coefficients. Table 2 presents the set of parameters that describe all the observed mode characteristics under the applied pressure. Figure 8 depicts the pressure dependence of the Raman frequencies that were generated by applying Equation 5 to the data presented in Table 2.

An interesting phenomenon of a phase transition at high pressure conditions has been observed (43). When the applied pressure exceeded 45 GPa, the GaN crystal became dark and the Raman signal disappeared. The researchers suggested that at a pressure of ~48 GPa, a

Table 2 The parameters of the pressure relation for the Raman modes (43)

Mode	ω_0 (cm^{-1})	σ_1 (cm^{-1}/GPa)	σ_2 (cm^{-1}/GPa^2)
$A_1(TO)$	531	4.06	−0.0127
$E_1(TO)$	560	3.68	−0.0078
$E_2^{(2)}$	568	4.17	−0.0136
$E_2^{(1)}$	144	−0.25	−0.0017

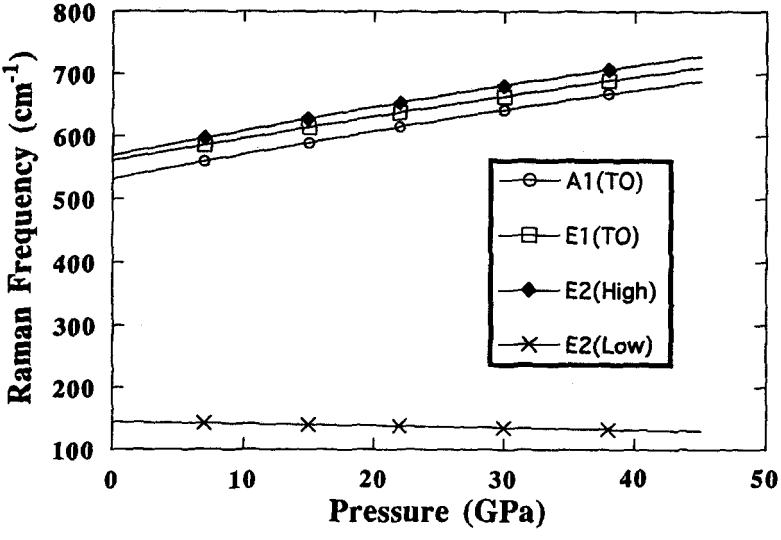

Figure 8 The pressure dependence of the Raman frequencies of WZ GaN. (Data from 43.)

phase transition might be taking place from the WZ stable structure to the NaCl structure.

Another mechanism that affects the Raman lineshape in GaN is the coupling of the phonons to the plasma oscillations of the free carriers (plasmons). Klein et al have developed a model that predicts the Raman lineshape for phonon-plasmon interactions (44). According to the model, when a material contains free carriers in an appreciable concentration, the Raman cross section may be modulated by two mechanisms. The first is the modulation of the Raman polarizability by the atomic displacement (deformation-potential mechanism), and the modulation via the longitudinal electric field of the carriers (electro-optic mechanism). The second mechanism is that of direct scattering events caused by the electronic-charge-density fluctuations. In SiC (44), GaP (45), and GaN (19), the scattering events due to the electronic-charge-density fluctuations are found to have a much smaller effect than the deformation-potential and the electro-optic mechanisms. Thus the electronic-charge-density fluctuations mechanism may be neglected. The equation of the Raman lineshape based on this model is rather complex and has been used to fit the data (46). However, the curve fit of the experimental data to the equation yields, among other physical parameters, the plasmon frequency ω_p from which the value of the concentration of free carriers n can be determined:

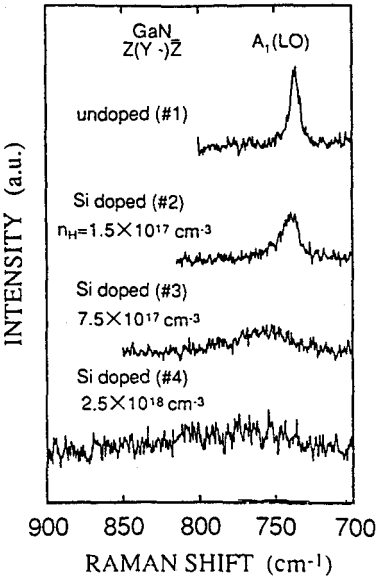

Figure 9 Raman spectra of the $A_1(LO)$ mode of GaN at several free carrier concentrations. (From 19.)

$$n = \frac{\omega_p^2 \epsilon_\infty m^*}{4\pi e^2}, \qquad 6.$$

where for a given material e is the electron charge, m* is the electronic effective mass, and ϵ_∞ is the high-frequency dielectric constant.

The determination of the concentration of free carriers via Raman spectroscopy is often more advantageous than that via electrical measurements because no contacts are required. The former technique has proven to be effective in the determination of the free carriers concentration in doped SiC (47) and doped GaP (46). Recently, Kozawa et al investigated the LO phonon-plasmon coupled modes in GaN (19). Figure 9 shows the Raman spectra of the $A_1(LO)$ mode at several carrier concentrations; here the Raman band shifts towards the high-frequency side and broadens with an increase in the carrier concentration. The spectra of the $A_1(LO)$ coupled mode as well as the model-predicted lineshape are presented in Figure 10. The inset to the figure lists the values of the fitting parameters among which is the plasmon frequency ω_p, from which the carrier concentration may be evaluated (via Equation 6, as described previously). Figure 11 shows the carrier concentration n calculated from the Raman data vs those obtained from the Hall measurements. As shown, the values of the concentrations obtained in both techniques agree.

Because of the difficulty in achieving high-quality cubic GaN sam-

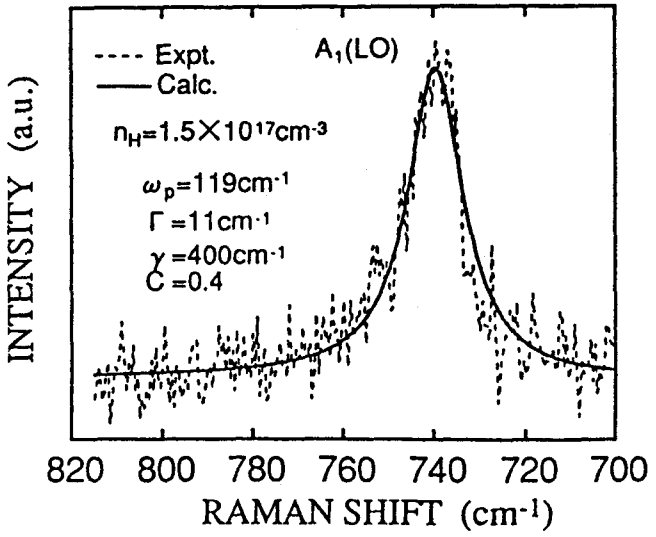

Figure 10 The experimental data and the calculated Raman lineshape of the $A_1(LO)$ mode of GaN. (From 19.)

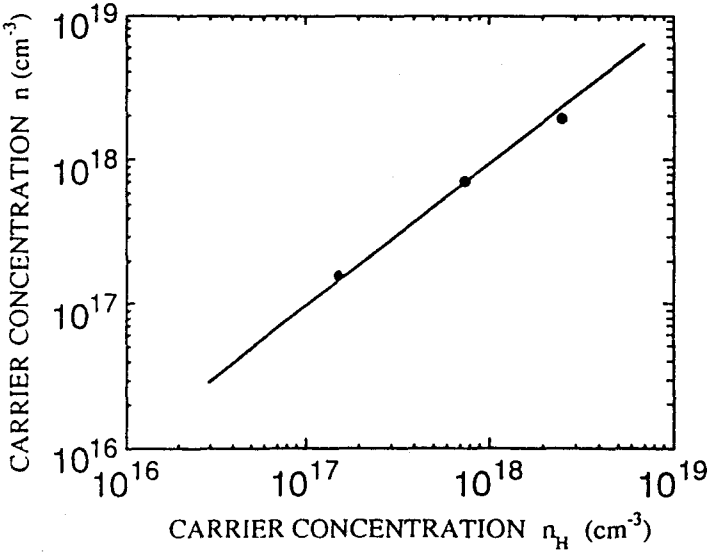

Figure 11 The free carrier concentration calculated from the Raman data vs the concentration n_H obtained from the Hall measurements. (From 19.)

ples, little information is available on the Raman characteristics of the cubic phases in contrast to the more well-researched hexagonal GaN. However, a few recent results have been reported in this area. Miyoshi et al have grown high-quality cubic zinc-blend GaN films on (100) GaAs substrates (48). The researchers observed the LO mode at 730 cm^{-1} and the TO mode at around 550 cm^{-1}. Humphreys et al have achieved both cubic and WZ GaN epitaxial films, which have been grown on (0001) sapphire substrates (49). The difference between growth temperatures of the substrates was suggested to give rise to the different observed phases. A Raman peak at ~740 cm^{-1} was also observed in the spectra and was attributed to the cubic phase of GaN. Lastly, recent calculations (50) predict the frequency of the Raman TO mode of the cubic zinc-blend structure to be 558 cm^{-1}.

One of the most promising materials for the fabrication of optoelectronic devices is the $A1_xGa_{1-x}N$ alloy series (51–54). The optical properties of the $Al_xGa_{1-x}N$ alloys are, to a large extent, unknown. The lack of information is due mainly to the difficulty of growing the material. The first to report the Raman characteristics of $Al_xGa_{1-x}N$ alloys were Hayashi et al (55). Their analysis was based on previous investigations of the optical phonons in other families of mixed crystals (56). A brief review of these fundamental antecedent results is given, followed by a discussion of the application to $Al_xGa_{1-x}N$.

Mixed crystals of the form $AB_{1-x}C_x$ are classified into two main classes according to the behavior of the $k \sim 0$ optical phonons (56). Figure 12 depicts the two classes, referred to as the one-mode and two-mode material, respectively. In general, if the frequencies of the AB and AC components differ greatly, a two-mode behavior is expected; if the frequencies of both components have proximate values, a one-mode behavior results. As can be seen in Figure 12*a*, for an intermediate composition x in the two-mode class of materials, two sets of frequencies have usually been observed in the spectra. One set of frequencies is due to the LO and TO modes of the lighter AB component, and the other set is due to the LO and TO modes of the heavier AC component. The frequencies of the two-mode material are not linear with x; moreover, the modes are degenerate at $x \sim 0$ and $x \sim 1$. The degenerate mode at $x \sim 1$ has been attributed to a local mode arising from a residual concentration of the B component present in the AC component. On the other hand, the degenerate mode at $x \sim 0$, which occurs in the composition region where AB is almost pure, has been regarded as a resonance gap-mode arising from residuals of C defects in the AB component.

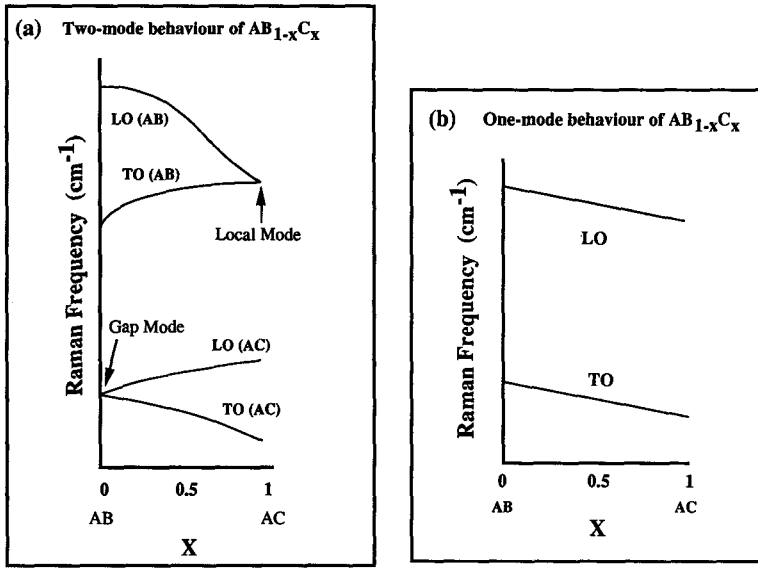

Figure 12 The two classes of mixed crystals: *(a)* two-mode type and *(b)* one-mode type material.

The phonons of the one-mode class of materials exhibit fundamentally different behavior than those of the two-mode materials. It can be seen in Figure 12*b* that only one set of LO and TO frequencies is present and that the frequencies vary linearly with the composition from the AB component to the AC component. In addition to the one-mode and two-mode classes of materials, an intermediate class exists that exhibits two-mode behavior over a certain composition range and one-mode behavior over the rest of the range. The intermediate type of behavior has been observed in some of the III-V crystals (57) including $AsGa_{1-x}In_x$, $GaAs_{1-x}Sb_x$, $SbGa_{1-x}In_x$, and $InAs_{1-x}Sb_x$.

Raman studies of $Al_xGa_{1-x}N$ films in the composition range $0 < x < 0.15$ have been recently described (55). Figures 13 and 14 present the Raman spectra and the frequencies as a function of composition, respectively. The 0.15 composition range studied in (55) corresponds to the range in Figure 12 where the AC (GaN) component is in an almost pure state. Therefore, if the $Al_xGa_{1-x}N$ film in this composition range is one-mode, then a linear dependence of the LO and TO modes on the composition is expected. Moreover, the slopes of the two lines should have the same sign. If the film is of a two-mode type, then the LO and TO dependence on composition is expected to be nonlinear

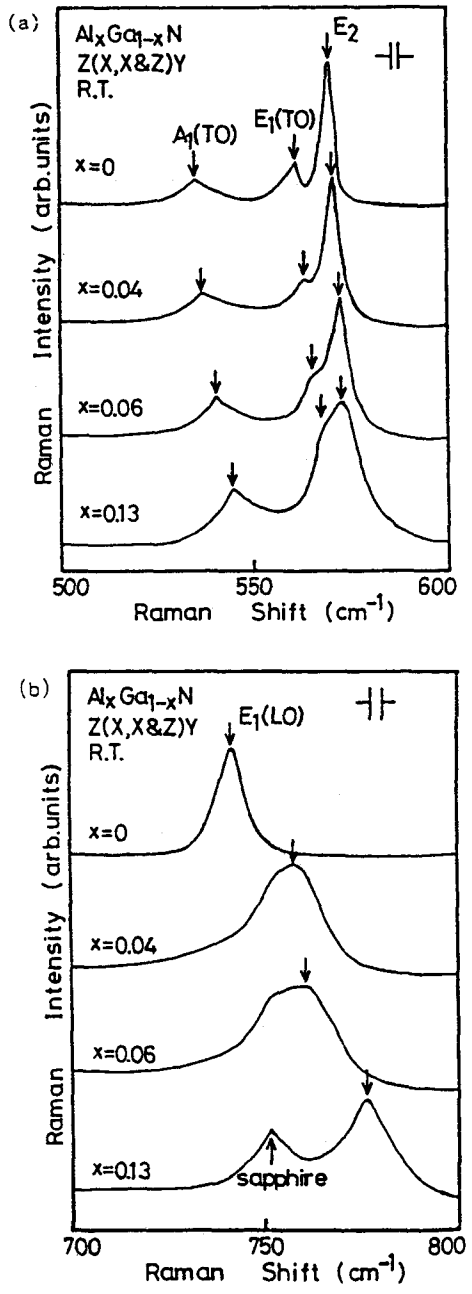

Figure 13 Raman spectra of *(a)* A_1(TO), E_1(TO), and E_2 modes and *(b)* E_1(LO) of $Al_xGa_{1-x}N$ at various compositions *x*. (From 55.)

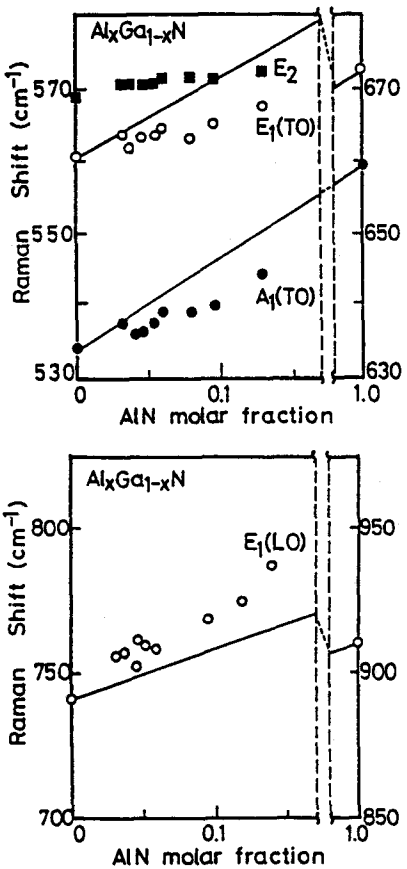

Figure 14 Compositional dependence of E_2, $E_1(TO)$, $A_1(TO)$, and $E_1(LO)$ modes of $Al_xGa_{1-x}N$. (From 55.)

and the slopes to be of opposite sign. Also, a local mode, due to residual concentration of Al atoms in the GaN matrix, should exist.

The $E_1(TO)$ and $E_1(LO)$ Raman frequencies, which have been investigated by Hayashi et al, have been shown to comply, according to the above criteria, with the one-mode behavior (55). As can be seen in Figure 14, both $E_1(T)$ and $E_1(LO)$ frequencies exhibit a linear increase (with a small deviation of unknown origin) with the Al composition, and no local mode arising from Al was observed.

ALUMINUM NITRIDE

In the following, a review of the Raman active modes of the wurtzite AlN is presented, and the effect of applied pressure on the Raman

Table 3 The Raman frequencies in units of cm^{-1} of the WZ aluminum nitride modes

$A_1(TO)$	$A_1(LO)$	$E_1(TO)$	$E_1(LO)$	$E_2^{(1)}$	$E_2^{(2)}$	Reference
614	893	673	916	252	660	58
607	—	—	924	241	660	15
659	888	671	895	—	—	59
667	910	667	910	—	655	60

frequencies, as well as the effect of oxygen impurity on the Raman characteristics, is discussed.

AlN, like GaN, in the stable state has a wurtzite crystal structure and belongs to the space group C_{6v}^4. The group theory predictions are essentially the same as described above (39). Table 3 lists the observed Raman frequencies of AlN single crystals (15, 58–60). As shown in the table, there is a large variance in the reported frequencies for a given mode. This variance may be attributed to the crystalline quality of the AlN samples (58).

Raman scattering studies of AlN crystals under pressure have been conducted by Perlin et al (15) and by Sanjurjo et al (59). The applied pressure was hydrostatic in the range of 0–14 GPA. Both groups observed that the Raman frequencies of the AlN modes increase almost linearly with applied pressure. The pressure dependence of the Raman frequency ω reported by Perlin et al (15) is of the form

$$\omega(cm^{-1}) = \omega_0 + \sigma_1 P + \sigma_2 P^2, \quad 7.$$

where P is the applied pressure in units of GPa, ω_0 is the Raman frequency in no-pressure conditions, and σ_1 and σ_2 are the pressure coefficients. A slightly different pressure dependence of the form

$$\omega(cm^{-1}) = \omega_0 + \sigma_1 P \quad 8.$$

was reported by Sanjurjo et al (59). Table 4 presents the set of parameters for Equations 7 and 8, describing the observed mode characteristics for both studies.

The high solubility of oxygen impurities in AlN has been shown to degrade the optical and thermal properties of the material (61–63). Moreover, it has been observed that a critical oxygen concentration exists past which the photoluminescence, thermal conductivity, and the unit-cell volume undergo a significant change in characteristics (61). Figure 15 shows the thermal resistance as a function of oxygen content (61–63). As is evident from the figure, at ~0.8 at % oxygen concentration, a change in the behavior of the thermal resistance occurs.

Table 4 The parameters of the pressure relation for the AlN Raman modes

Mode	ω_0 (cm^{-1})	σ_1 (cm^{-1}/GPa)	σ_2 (cm^{-1}/GPa^2)	Reference
$A_1(TO)$	607	4.63	−0.01	15
$E_1(LO)$	924	1.67	0.27	15
$E_2^{(2)}$	660	3.99	0.035	15
$A_1(TO)$	659	4.97	—	59
$A_1(LO)$	888	3.8	—	59
$E_1(TO)$	671	4.84	—	59
$E_1(LO)$	895	4.0	—	59

The influence of the oxygen impurity concentration on the Raman lineshape, as investigated by McNeil et al, showed a trend similar to that above (58). Figure 16 presents the Raman linewidth as a function of oxygen concentration: at the critical concentration of ~0.8 at %, a transition in the behavior of the linewidth is noted. The observed phenomenon of a critical oxygen concentration has been attributed to

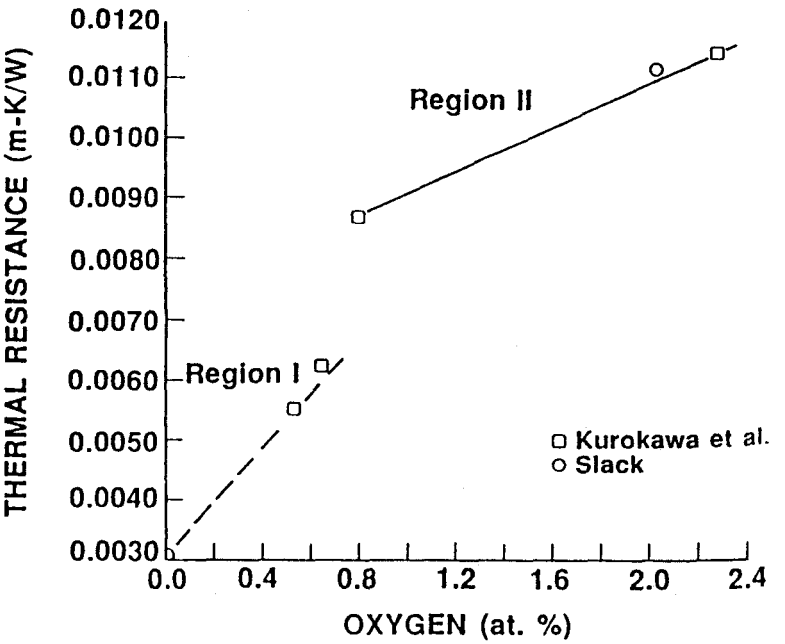

Figure 15 Thermal resistance of AlN as a function of oxygen concentration. (From 61.)

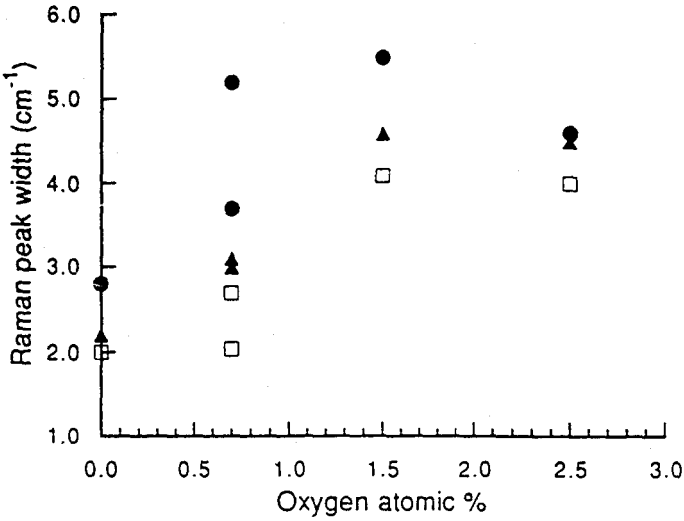

Figure 16 Raman linewidth of AlN vs oxygen concentration for E_1 mode *(square)*, A_1 mode *(circle)*, and E_2 mode *(triangle)*. (From 58.)

a change in the structure of the oxygen defect; up to 0.8 at %, the oxygen impurity is a point-like defect, and above that concentration the oxygen is in the form of an extended defect (58, 61).

BORON NITRIDE

Boron nitride can have a cubic, hexagonal, wurtzite, rhombohedral, or turbostratic structure (13). Among these various structures, only the zinc-blend cubic BN (c-BN) and the hexagonal BN (h-BN) have been investigated via Raman spectroscopy because of the high-quality crystals achieved for these structures.

The following presents a review of Raman investigations of c-BN and h-BN. The bonding-anisotropy of the h-BN, as well as the effect of the crystallite size on the Raman modes, is discussed. Lastly, a review of the effect of high pressure and temperature on the Raman frequencies of h-BN and c-BN is presented.

The c-BN belongs to the T_d^2 space group and has LO and TO Raman-active modes (60). The h-BN, on the other hand, belongs to the D_{4h}^6 space group and has two E_{2g} Raman-active modes (64). Table 5 lists the Raman frequencies of the two structures (60, 65).

The large variance in the Raman frequencies of h-BN (52 and 1366

Table 5 The Raman frequencies of the h-BN and the c-BN

Frequency of h-BN (cm^{-1})		Frequency of C-BN (cm^{-1})	
Low Frequency:	52.5[a]	LO:	1304.0[b]
High frequency:	1366.0[a]	TO:	1056.0[b]

[a] Reference 65.
[b] Reference 60.

cm^{-1}) is due to the large anisotropy of the bonding configurations of this material. Figure 17 shows the crystal structure of h-BN: The structure consists of hexagonal planes of boron atoms bonded to nitrogen atoms. Within any plane there is a strong sp^2 bonding between the boron and the nitrogen atoms; however, only a weak van der Waals bonding exists between planes. The low-frequency mode at 52 cm^{-1} is due to vibrations originating from adjacent planes sliding against each other (rigid-layer shear mode), whereas the high-frequency mode at 1366 cm^{-1} is due to in-plane vibrations between the boron and nitrogen atoms.

The effect of the crystallite domain size on the high-frequency 1366 cm^{-1} Raman mode of h-BN has been previously investigated (17). The

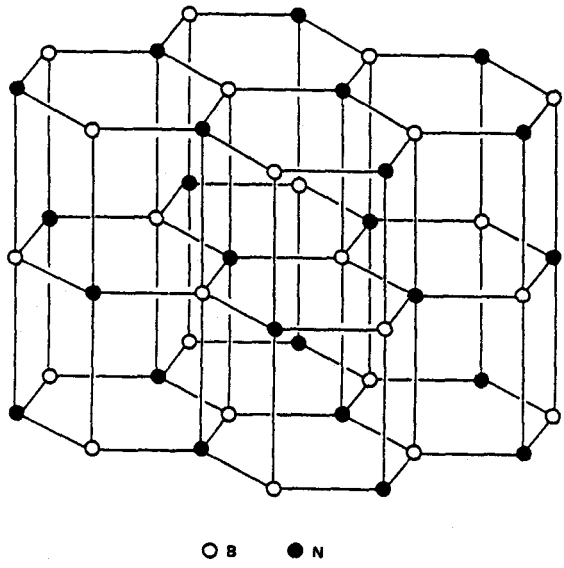

Figure 17 The crystal structure of the h-BN. (From 17.)

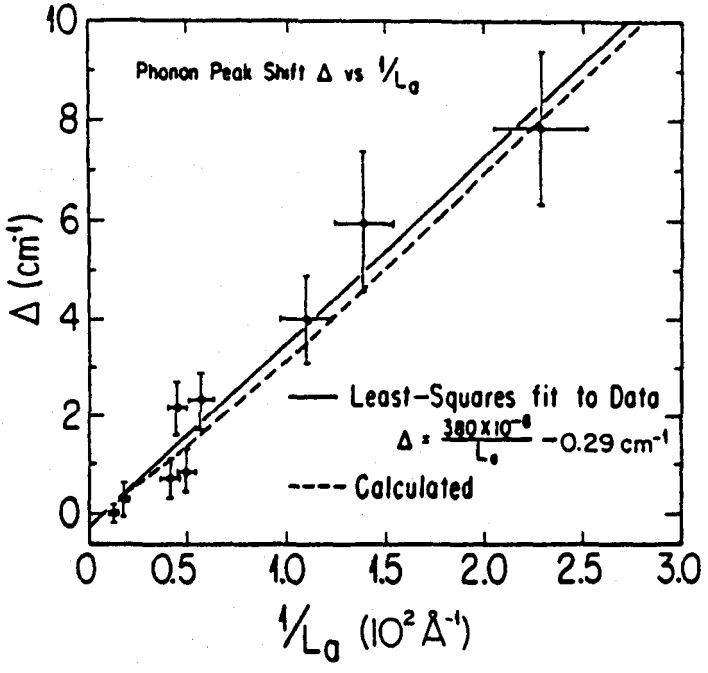

Figure 18 The dependence of the peak position of the high-frequency E_{2g} mode of h-BN vs 1/*L*. The solid line represents the Raman data, whereas the dashed line represents the calculated peak position using the phonon-confinement model. (From 17.)

Raman measurements indicated that the Raman line shifted to higher frequency, broadened, and became asymmetric as the crystallite size decreased. It was shown (17) that the observed Raman characteristics can be explained via the phonon-confinement model (see Equation 4). Figure 18 depicts the experimental and calculated dependence of the Raman peak position on the crystallite size *L*. The experimental data in Figure 18 agree with the model.

The shift of the h-BN Raman line to higher frequency with decreasing confinement size is a manifestation of the unusual dispersion curves that h-BN is predicted to have; the phonon frequency of the highest branch is not a maximum at the Γ point (17). For most crystalline solids the reverse is true; a decrease in the Raman shift (of the highest-frequency nonpolar mode) with decreasing crystallite size is expected [as occurs in the case of silicon (36) and cluster diamond (38)].

The effect of applied pressure (in the range 0–11 GPa) on the Raman modes of h-BN has been studied by Kuzuba et al (66). The researchers investigated the dependence of the high-frequency 1366 cm^{-1} and low-

frequency 52 cm^{-1} modes on the pressure in order to study the anisotropy of the force constants. The high- as well as the low-frequency Raman modes were observed to increase with the applied pressure. However, the mode frequencies were found to increase with different rates, implying different pressure coefficients of 5 cm^{-1}/GPa for the low-frequency mode and 4 cm^{-1}/GPa for the high-frequency mode. Furthermore, the change in force constant (from the atmospheric value to the value at 11 GPa) of both modes was calculated. It was found that the force constant of the low-frequency mode increased by a factor of 4, whereas that of the high-frequency mode increased by only 6%. The results of Kuzuba reflect the strong anisotropy of the force constants in h-BN.

Recently the pressure dependence of the LO and TO Raman modes of c-BN have been investigated (59). The pressure coefficient for the LO and TO was found to be 3.45 and 3.39 cm^{-1} GPa, respectively. In this pressure range, the pressure dependence P of the Raman frequency ω has been determined to follow the linear relation (59)

$$\omega_{LO} = 1305 + 3.45P$$

$$\omega_{TO} = 1054 + 3.39P.$$

The results of the pressure dependence studies indicate that the pressure coefficients of c-BN are smaller than those of h-BN, implying that the Raman modes of c-BN comply less to stress than those of h-BN.

In addition to yielding information about the stress state, Raman spectroscopy is also a powerful tool in the study of the thermal properties of solids (67–69). Recently, the temperature dependence (in the range 300–1830K) of the TO and LO Raman modes of c-BN has been investigated by Herchen & Cappelli (16). The study indicated that the Raman frequency ω of both modes decrease with increasing temperature:

$$\omega = \omega_0 - a_1 T - a_2 T^2,$$

where $\omega_0 = 1060.6$ cm^{-1}, $a_1 = 0.010$ cm^{-1}/K, and $a_2 = 1.42 \times 10^{-5}$ cm^{-1}/K^2 for the TO mode, and $\omega_0 = 1307.6$ cm^{-1}, $a_1 = 0.003$ cm^{-1}/K, and $a_2 = 1.46 \times 10^{-5}$ cm^{-1}/K^2 for the LO mode. Figure 19 presents the temperature dependence of the Raman frequencies of c-BN. The temperature behavior of the Raman frequency of crystalline diamond is also shown in the figure; it is evident that the temperature dependence of both materials is similar. The frequency change between room temperature and 1800 K was calculated for c-BN to be 5.6 and 3.8% for the TO and LO modes, respectively, and 3.4% for diamond

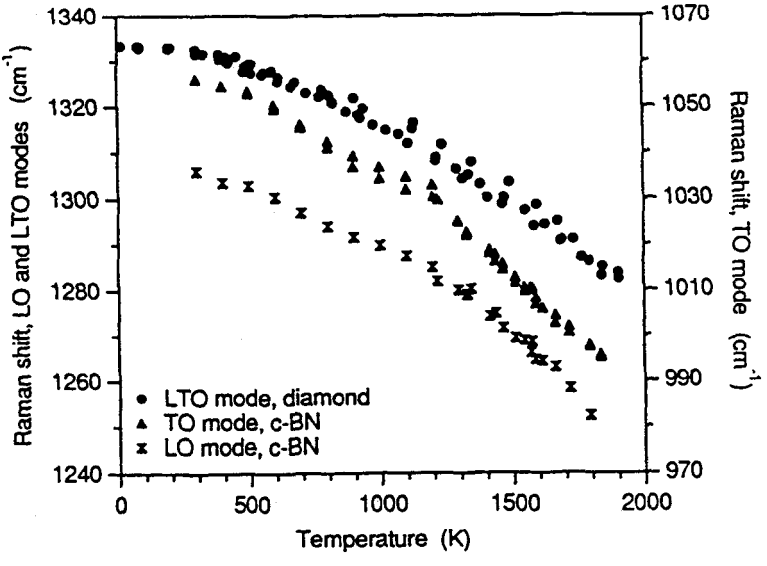

Figure 19 The temperature dependence of the Raman frequency of diamond and c-BN. (From 16.)

(16). The similar temperature dependence of both materials implies that c-BN has thermal properties comparable to that of diamond.

To date no temperature dependence studies have been conducted on the anisotropy of the Raman frequencies of h-BN. However, the temperature response (in the range 300–2325 K) of the high-frequency E_{2g} Raman mode of h-BN has been studied by Exarhos & Schaaf (70). The temperature dependence of the Raman frequency ω and the linewidth $\Delta\omega$ were shown to follow the relations:

$$\omega^2 = 1372^2 - 71.98T - 1.197 \times 10^{-2}T^2$$

$$\Delta\omega = 7.67 + 3.62 \times 10^{-3}T + 5.22 \times 10^{-6}T^2.$$

In addition, Exarhos & Schaaf outlined a method to calculate the intralamellar thermal expansion coefficient from the Raman analysis; the value was calculated to be 3.5×10^{-6} deg^{-1} (70).

CONCLUDING REMARKS

The Raman effect arises from the interaction of light with matter; as such, Raman spectroscopy is a nondestructive and powerful tool in the study of lattice dynamics. The various investigations reviewed here

demonstrate the utility of Raman spectroscopy in characterizing the bond configuration, stress state, and thermal stability of wide-bandgap semiconductors. Moreover, through Raman spectroscopy valuable information may be obtained about the impurities and structural defects present in a crystal matrix. Although significant progress has been made in understanding the crystal dynamics of the stable structure of GaN, AlN, and BN, as well as diamond films, the investigation of the phonon characteristics of the unstable states and novel mixed alloys are still at the initial stages.

Literature Cited

1. Davis RF. 1991. *Proc. IEEE* 79: 702–12
2. Edgar JH. 1992. *J. Mater. Res.* 7: 235–52
3. Kubota K, Kobayashi Y, Fujimoto K. 1989. *J. Appl. Phys.* 66:2984–88
4. Nemanich RJ. 1991. *Annu. Rev. Mater. Sci.* 21:535–58
5. Ravi KV. 1993. *Mater. Sci. Eng. B* 19: 203–27
6. Morkoc H, Strite S, Gao GB, Lin ME, Sverdlov B, Burns M. 1994. *J. Appl. Phys.* 76:1363–98
7. Badzian AR, Badzian T, Roy R, Messier R, Spear KE. 1988. *Mater. Res. Bull.* 23:531–48
8. Collins AT, Kamo M, Sato Y. 1990. *J. Mater. Res.* 5:2507–13
9. Ruan J, Choyke WJ, Partlow WD. 1991. *J. Appl. Phys.* 69:6632–36
10. Robins LH, Cook LP, Farabaugh EN, Feldman A. 1989. *Phys. Rev. B* 39: 13367–77
11. Zhu W, Badzian AR, Messier R. 1989. *J. Mater. Res.* 4:659–63
12. Williams BE, Glass JT, Davis RF, Kobashi K, Horiuchi T. 1988. *J. Vac. Sci. Technol. A* 6:1819–20
13. Edgar JH, ed. 1994. *Properties of Group III Nitrides.* London: INSPEC
14. Matsuoka T. 1992. *J. Cryst. Growth* 124:433–38
15. Perlin P, Polian A, Suski T. 1993. *Phys. Rev. B* 47:2874–77
16. Herchen H, Cappelli MA. 1993. *Phys. Rev. B* 47:14193–99
17. Nemanich RJ, Solin SA, Martin RM. 1981. *Phys. Rev. B* 23:6348–56
18. Berenholc J, Chervin JC, Moustakas TD. 1995. *Phys. Rev. Lett.* 75:296
19. Kozawa T, Kachi T, Kano H, Taga Y, Hashimoto M, et al. 1994. *J. Appl. Phys.* 75:1098–101
20. Neugebauer J, Walle CGVD. 1994. *Phys. Rev. B* 50:8067–70
21. Pankove JI, Hutchby JA. 1976. *J. Appl. Phys.* 47:5387–90
22. Nemanich RJ, Solin SJ. 1979. *Phys. Rev. B* 20:392–401
23. Shroder RE, Nemanich RJ, Glass JT. 1990. *Phys. Rev. B* 41:3738–45
24. Nemanich RJ, Glass JT, Lucovsky G, Shroder RE. 1988. *J. Vac. Sci. Technol. A* 6:1783
25. Loudon R. 1964. *J. Phys.* 26:677
26. Wada N, Solin SA. 1981. *Phys. B* 105: 353–56
27. Bergman L, Stoner BR, Turner KF, Glass JT, Nemanich RJ. 1993. *J. Appl. Phys.* 73:3951–57
28. Bergman L, McClure MT, Glass JT, Nemanich RJ. 1994. *J. Appl. Phys.* 76: 3020–27
29. Bergman L, Nemanich RJ. 1995. *J. Appl. Phys.* 78:6709–19
30. Freitas JA, Butler JE, Strom U. 1990. *J. Mater. Res.* 5:2502–6
31. Windischmann H, Epps GF, Cong Y, Collins RW. 1991. *J. Appl. Phys.* 69: 2231–37
32. Borer WJ, Mitra SS, Namjoshi KV. 1971. *Solid State Commun.* 9:1377
33. Di Bartolo B. 1969. *Optical Interactions in Solids.* New York: Wiley & Sons
34. Ager JW, Veirs DK, Rosenblatt GM. 1991. *Phys. Rev. B* 43:6491–99

35. Campbell IH, Fauchet PM. 1986. *Solid State Commun.* 58:739
36. Fauchet PM, Campbell IH. 1988. *Crit. Rev. Solid State Mater. Sci.* 14: S79–101
37. Tubino R, Birman JL. 1977. *Phys. Rev. B* 15:5843
38. Yoshikawa M, Mori Y, Obata H, Maegawa M, Katagiri G, et al. 1995. *Appl. Phys. Lett.* 67:694–96
39. Arguello CA, Rousseau DL, Porto SPS. 1969. *Phys. Rev.* 181:1351–63
40. Manchon DD, Barker AS, Dean PJ, Zetterstrom RB. 1970. *Solid State Commun.* 8:1227–31
41. Cingolani A, Ferrara M, Lugara M, Scamarcio G. 1986. *Solid State Commun.* 58:823–24
42. Murugkar S, Merlin R, Botchkarev A, Salvador A, Morkoc H. 1995. *J. Appl. Phys.* 77:6042–43
43. Perlin P, Carillon CJ, Itie JP, Miguel AS, Grzegory I, Polian A. 1992. *Phys. Rev. B* 45:83–89
44. Klein MV, Ganguly BN, Colwell PJ. 1972. *Phys. Rev. B* 6:2380–88
45. Hon DT, Faust WL. 1973. *Appl. Phys.* 1:241–56
46. Irmer G, Toporov VV, Bairamov BH, Monecke J. 1983. *Phys. State Solid B* 119:595–603
47. Yugami H, Nakashima S, Mitsuishi A, Uemoto A, Shigeta M, et al. 1987. *J. Appl. Phys.* 61:354–58
48. Miyoshi S, Onabe K, Ohkouchi N, Yaguchi H, Ito R, et al. 1992. *J. Cryst. Growth* 124:439–42
49. Humphreys TP, Sukow CA, Nemanich RJ, Posthill JB, Rudder RA, et al. 1990. *Mater. Res. Soc. Proc.* 162: 531–63
50. Miwa K, Fukumoto A. 1993. *Phys. Rev. B* 48:7897–902
51. Hagen J, Metcalfe RD, Wickenden D, Clark W. 1978. *J. Phys. C: Solid State Phys.* 11:L143–46
52. Murakami H, Asahi T, Amano H, Hiramatsu K, Sawaki N, Akasaki I. 1991. *J. Cryst. Growth* 115:648–51
53. Khan MA, Skogman RA, Schulze RG, Gershenzon M. 1983. *Appl. Phys. Lett.* 43:492–94
54. Yoshida S, Misawa S, Gonda S. 1982. *J. Appl. Phys.* 53:6844–48
55. Hayashi K, Itoh K, Sawaki N, Akasaki I. 1991. *Solid State Commun.* 77: 115–18
56. Chang IF, Mitra SS. 1968. *Phys. Rev.* 172:924–33
57. Lucovsky G, Chen MF. 1970. *Solid State Commun.* 8:1397
58. McNeil LE, Grimsditch M, French RH. 1993. *J. Am. Ceram. Soc.* 76: 1132–36
59. Sanjurjo JA, Cruz EL, Vogl P, Cardona M. 1983. *Phys. Rev. B* 28: 4579–84
60. Brafman O, Lengyel G, Mitra SS, Gielisse PJ, Plendl JN, Mansur LC. 1968. *Solid State Commun.* 6:523–26
61. Harris JH, Youngman RA, Teller RG. 1990. *J. Mater. Res.* 5:1763–73
62. Slack GA. 1973. *J. Phys. Chem. Solids* 34:321
63. Kurokawa Y, Utsumi K, Takamizawa H. 1988. *J. Am. Ceram. Soc.* 71:588
64. Geick R, Perry CH, Rupprecht G. 1966. *Phys. Rev.* 146:543–47
65. Kuzuba T, Era K, Ishii T, Sato T. 1978. *Solid State Commun.* 25:863–65
66. Kuzuba T, Sato Y, Yamaoka S, Era K. 1978. *Phys. Rev. B* 18:4440–43
67. Balkanski M, Wallis RF, Haro E. 1983. *Phys. Rev. B* 28:1928–34
68. Hart TR, Aggarwal RL, Lax B. 1970. *Phys. Rev. B* 1:638–42
69. Zouboulis ES, Grimsditch M. 1991. *Phys. Rev. B* 43:12490–93
70. Exarhos GJ, Schaaf JW. 1991. *J. Appl. Phys.* 69:2543–48

Annual Review of Materials Science
Volume 26, 1996

CONTENTS